Optimising Spherical Sampling for Far-Field Antenna Measurements

A Comparative Study to Minimise Measurement Time While Maintaining Accuracy

by

Sven Lemsom and Sitti Romijn

In partial fulfilment of the requirements for the degree of

Bachelor of Science

In Electrical Engineering

Supervisors:

Dr. D. Cavallo,
Ir. R. G. Tapia Barroso

June 26, 2025

Delft University Of Technology
Faculty of Electrical Engineering, Mathematics and Computer Science
Electrical Engineering Programme

TU Delft

Abstract

This thesis aims to further study the optimal algorithm for data acquisition in the far field region of an electromagnetic field radiated by an antenna. This was done as a part of a larger project where the aim was to design and test an antenna measurement setup, which utilises a robotic arm to perform the measurements. Various sampling algorithms were implemented and tested on simulated analytic field patterns, performed using MATLAB. The sampling grids used in simulations were the equiangular, Fibonacci and Gauss-Legendre grid. The performance of these algorithms were evaluated, using the number of samples as a way to measure their efficiency and the calculated directivity as a way to measure the accuracy. Then, they were validated using measurements made using rectangular horn antennas in combination with the measurement setup utilising the robotic arm. Then from these measurements a visualisation of the radiation patterns were generated. In the end the results verify that the proposed algorithms will work as an efficient and accurate algorithm for data acquisition and will provide a valid sampling method to be used in the final measurement setup. The Gauss-Legendre grid proved more efficient for measuring the field and calculating the directivity, while maintaining the same levels of accuracy as the equiangular grid.

Preface

The last eight weeks we have been working towards designing and testing an antenna measurement setup for our Bachelor End Project (BEP). We aspired in this project to use our knowledge gained throughout our bachelor Electrical Engineering to complete this task and to deliver a product that lives up to the standard present in the field of Electrical Engineering. We did this together with Guus Hak, Tom Rietjens, Huib Maas, Fabian Wichman, Danylo Zavoloko, and Matthieu Gillain. Whom without this project would not have succeeded and we would like to thank them for a successful collaboration.

We would also like to thank our daily supervisor, ir. Roderick Tapia Barroso, for all his help and advice and especially for giving us a clear view of the task at hand. And to our supervisors, prof. dr. N. Llombart and dr. D. Cavallo, for their feedback and advice. Also a special thanks to ir. Jingling Geng, for helping with the measurements. Finally a thanks to all people who contributed or helped in a direct or indirect way throughout this project and are not named here.

Contents

Chapter 1
Introduction

1.1 Background

Modern wireless communication and sensing systems are now widespread across numerous applications and are fundamentally dependent on the performance of their antennas. As such, precise characterisation of antenna behaviour is essential during both the design and validation phases. Traditionally, these measurements are conducted in controlled environments such as anechoic chambers, using static or manually operated setups. While these methods are reliable, they are often time-consuming and lack the flexibility required for testing advanced or high-frequency antenna systems.

In recent years, robotic systems have gained attention as a means to automate and enhance antenna measurement procedures. Boehm et al. [1] were among the first to demonstrate the viability of robotic arms for millimetre-wave antenna characterisation, enabling accurate and repeatable measurements across a wide spatial range. More recently, Meng et al. [2] developed a robotic measurement system capable of characterising radiation patterns in both near-field and far-field regions across a 6–110 GHz frequency range.

Expanding on all of this, Gordon [3] provides an overview of contemporary robotic measurement approaches, noting their adaptability and effectiveness when paired with advanced alignment and control techniques.

Lewis et al. [4] further explored the evolution from traditional measurement environments to more modern, robotic-based systems. Their analysis highlights not only the improvements in efficiency and measurement consistency, but also the potential of robotic setups to support dynamic and reconfigurable testing scenarios, such as characterising adaptive antennas or performing measurements under changing operational conditions.

1.2 Project Objective

The primary objective of this project is to develop an automated antenna measurement system based on a robotic arm for the Terahertz Sensing group, capable of acquiring near-field and far-field radiation patterns efficiently and accurately. The Terahertz Sensing group conducts research on antennas, among other topics. This requires the ability to perform antenna measurements for characterisation purposes.

The system must integrate a vector network analyser (VNA) for electromagnetic field acquisition and must enable the characterisation of antennas. A schematic of the entire system is given in Figure 1.1. The end goal is to extract key antenna parameters, including the far-field radiation pattern, total radiated power and directivity.

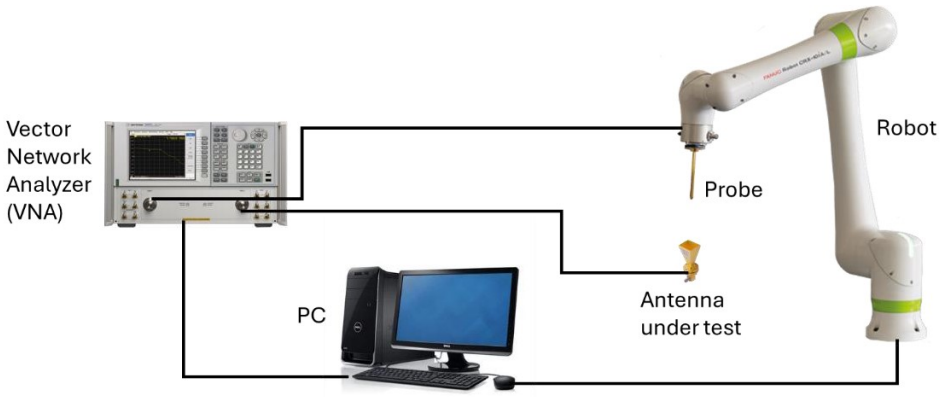

Figure 1.1: Schematic of the entire system.

The project is carried out by a team of eight Bachelor's thesis students, divided into four subgroups, each responsible for a core component of the system:

- **Subgroup 1** focuses on automating the robotic arm to follow different trajectories and polarisations, ensuring smooth motion and minimising abrupt positional changes. They are also responsible for optimising the motion path to improve measurement efficiency and continuity.
- **Subgroup 2** is tasked with developing a user-friendly software interface that allows users to configure, execute, and monitor antenna measurements. Their work involves integrating hardware and software subsystems and performing tests to analyse phase errors potentially introduced by robotic motion.
- **Subgroup 3** develops the sampling algorithm for far-field spherical measurements. The subgroup explores alternative spherical sampling strategies to reduce the number of acquisition points without compromising measurement accuracy, addressing the inefficiencies of conventional angular grids.
- **Subgroup 4** investigates near-field to far-field transformation techniques. Using the equivalence theorem and superposition principle, they aim to enable accurate far-field estimation based on near-field measurements, particularly relevant for high-frequency antennas where far-field distances are impractically large.

Together, these components form a complete and adaptable measurement system suitable for characterising a wide range of antenna types, with a particular focus on efficiency, modularity, and precision.

The remainder of this thesis presents the work of Subgroup 3. More specifically, a simulation-based trade-off study is conducted, which investigates the relationship between the number of far-field sampling points and the resulting measurement accuracy.

1.3 State-of-the-Art Analysis

Accurate far-field characterisation of antennas often requires measurements taken over a few cuts of a spherical surface surrounding the antenna under test (AUT). However, the sampling of the full sphere is needed for calculating the directivity, which depends on the total radiated power. The spatial distribution of sampling points on this sphere significantly impacts the efficiency of the measurement process in terms of duration and accuracy [5]. Traditional spherical grids, such as the theta-phi grid, defined in terms of equiangular steps in θ and ϕ, as shown in Figure 1.2a, result in non-uniform point densities, particularly near the poles. This leads to redundant measurements in some regions and under-sampling in others, making the method inefficient for high-resolution scans.

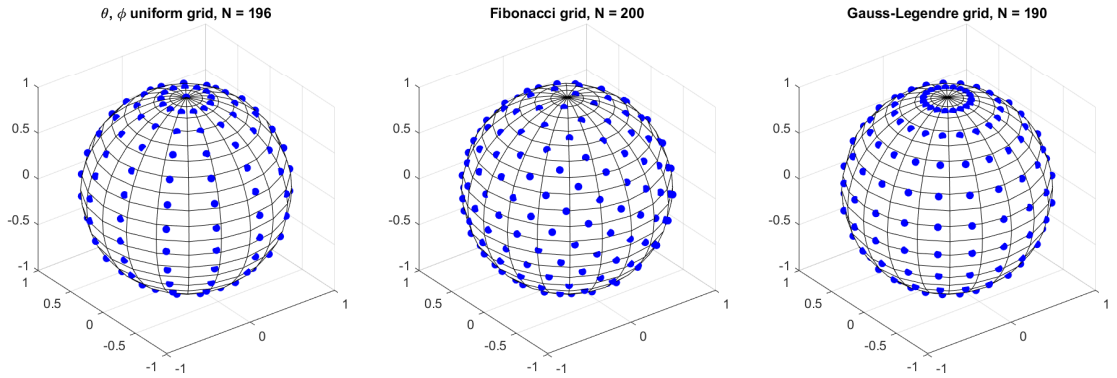

(a) (b) (c)

Figure 1.2: Different sampling grids, with the θ-ϕ grid in (a), the Fibonacci grid in (b) and the Gauss-Legendre in (c).

One well-known issue with the equiangular theta-phi grid is the clustering of points near the poles. This not only leads to oversampling in those regions but also increases the total number of measurements required to achieve a given accuracy. To mitigate this, more uniform sampling schemes have been proposed, including equidistant point distributions such as the Fibonacci grid [6], [7]. The Fibonacci grid distributes points along a spiral on the sphere's surface, where the angular increment between successive points is derived from the golden angle, based on the golden ratio. This results in a near-uniform distribution that reduces clustering and ensures more consistent spatial coverage [6], [7], [8].

Another important aspect of spherical sampling is numerical integration, especially when computing antenna parameters such as total radiated power or directivity, which require surface integration over the sphere. For non-uniform grids, this often involves applying weighting functions to compensate for variations in sampling density. In contrast, approximately uniform-area grids, like the Fibonacci lattice, can simplify integration by reducing the variance in surface element size, which can also improve numerical stability and reduce computation time [7], [8]. González [8] evaluated the error associated with measuring the area of spherical caps randomly positioned on the sphere. This analysis showed that the Fibonacci grid consistently produced lower maximum and average errors compared to latitude–longitude grids with the same number of points. Furthermore, the area errors in the Fibonacci grid were more uniformly distributed, making it a robust choice for applications requiring reliable numerical integration across the sphere.

Beyond equidistant approaches, other sampling schemes have been explored. For instance, Ahmed and Khalid [5] proposed the usage of a couple of different sampling schemes developed for the band-limited signals to sample the antenna radiation patterns. They considered the iso-latitude sampling schemes such as equiangular [9], Gauss-Legendre [10] and optimal-dimensionality [11]. These schemes allow for accurate reconstruction of antenna radiation patterns by using spherical harmonic transforms. They offer very low reconstruction errors and are well-suited for applications that need precise results without requiring a large number of samples.

1.4 Contribution

Far-field measurements are typically taken over a limited number of angular cuts. However, the robotic arm measurement setup developed during this Bachelor End Project enables efficient full-sphere measurements. This allows for accurate integration over the entire sphere and facilitates the calculation of key antenna parameters, such as directivity. As accurate results require a large number of acquisition points, it is essential to investigate sampling schemes that minimise the number of required measurements while maintaining sufficient accuracy.

To address this, various spherical sampling methods are investigated in this thesis, with a focus on analysing the trade-off between the number of sampling points and the resulting measurement accuracy. The proposed methods are validated through measurements of a test antenna using the robotic arm system. As a result, a more efficient sampling scheme than the traditional theta–phi grid is identified.

1.5 Thesis Outline

This thesis consists of five more chapters. In Chapter 2 the Programme of Requirements will be presented, which defines the functional and technical specifications for this project.

Chapters 3 and 4 cover the theoretical background necessary to understand the study. Chapter 3 presents the fundamental antenna theory relevant to far-field measurements, while Chapter 4 contains a detailed discussion of various spherical sampling schemes. Special attention is given here to the equiangular theta-phi grid, the Fibonacci grid, and the Gauss-Legendre quadrature.

Chapter 5 presents the core of the thesis: a trade-off study based on simulations in MATLAB. Section 5.1.1 discusses the trade-off between the number of points on the sphere and the accuracy, while Section 5.1.2 investigates the truncation behaviour.

Chapter 6 validates the findings of the simulation study through an experiment. It outlines the practical setup used to validate the Gauss-Legendre sampling method and presents the measured data and outcomes, offering insights into the performance under realistic conditions.

Finally, Chapter 7 concludes the thesis with a summary of the key findings, a reflection on the achieved objectives, and recommendations for future work.

Chapter 2
Programme of Requirements

This chapter outlines the Programme of Requirements for the automated antenna radiation measurement system using a 6-axis robotic arm. The need for such a system arises from the limitations of traditional antenna measurement setups, which typically consist of one or two turntables on which antennas are mounted. For high-frequency measurements, frequency extenders are often mounted directly with the antennas to minimise signal loss. By integrating a robotic arm with the antenna and relevant instrumentation (e.g. a Vector Network Analyser or *VNA*), this system aims to provide flexible, accurate, and repeatable antenna measurements in both near-field and far-field conditions.

The overall system will be developed collaboratively by four subgroups of students, each focusing on distinct but interconnected functionalities. The following sections describe the system-level requirements and the specific goals and constraints for Subgroup 3, which is focused on the spherical far-field measurements.

2.1 Requirements for the Entire System

Functional requirements

1.1 The system must be able to control the 6-axis robotic arm.

1.2 The system must provide a user interface (UI) for controlling the robotic arm, initiating measurements, keeping track on the progress of the measurements and visualising the measurement results.

1.3 The system must be able to characterise an antenna in terms of its 2D and 3D radiation pattern, total radiated power, directivity and gain.

1.4 The system must be able to perform spherical far-field measurements.

1.5 The system must be able to perform planar near-field measurements.

1.6 The system must be able to apply near-to-far-field transformations.

1.7 The system must support integration and synchronised control of the VNA and robotic arm.

1.8 The system must store raw and processed measurement data with options for data export.

System requirements

2.1 The robotic arm must support smooth and continuous movement across predefined spherical and planar scanning patterns.

2.2 The measurement system must ensure signal integrity during motion, minimising vibration-induced errors.

2.3 The robot control interface must allow user-defined scanning parameters.

2.4 The robot must operate safely within the defined mechanical limits to avoid collisions with the antenna or other objects.

2.5 The entire measurement cycle, from setup to data visualisation, must be executable via the user interface.

2.6 The system must be modular and scalable for future extensions.

Development requirements

3.1 All software must be developed in MATLAB.

3.2 The code must follow modular programming practices to allow for integration with other subsystems.

2.2 Requirements for Subgroup 3

The goal of Subgroup 3 is to develop a robust and accurate algorithm for spherical far-field data acquisition that enables calculation of antenna performance metrics such as total radiated power and directivity. Special focus is placed on optimising sampling schemes to reduce acquisition time while maintaining accuracy.

Functional requirements

A.1 The subsystem must calculate the radiated power and directivity from sampled electric far-field data (see Section 3.5 on how the electric field is measured).

A.2 The system must be able to generate 2D and 3D visualisations of radiation patterns based on sampled data.

A.3 Multiple sampling methods for data acquisition must be compared, including:

- Uniform sampling in θ and ϕ (see Figure 1.2a),
- Fibonacci spiral distribution (see Figure 1.2b),
- Gauss–Legendre quadrature (see Figure 1.2c).

A.4 The performance of acquisition algorithms must be evaluated as a function of the number of sampling points and acquisition time.

A.5 The subsystem must validate results using known analytical formulas for a uniform rectangular current distribution.

System requirements

B.1 Sampling grid configurations must be parameterisable by the user (e.g., angular resolution, number of points).

B.2 The subsystem must support coordinate transformations (spherical to Cartesian and vice-versa) for robot integration.

B.3 The subsystem must generate a list of measurement points that can be interpreted by the robotic control interface.

B.4 The subsystem must be able to truncate the grid due to limited angular range of the robotic system.

B.5 The subsystem must be testable in isolation via simulated field data.

Chapter 3
Antenna Theory

This chapter presents the fundamental antenna theory on which this thesis is based. It discusses multiple important concepts, such as the (Fraunhofer) far-field region, radiation pattern and directivity.

3.1 Far-Field Region

The space around the antenna can be divided into three different regions based on the distance from the antenna and the behaviour of the electromagnetic fields: the *reactive near-field*, the *radiating near-field* (also known as the Fresnel region) and the *far-field* or (*Fraunhofer region*) [12].

For each region, a radiated wave has different field structures. In the far-field, it approximates a plane wave, which means that at any point in the far-field of an antenna the electric-field strength is the same as that of the wave and its direction of propagation is approximately radial, pointing outward from the antenna [12].

The boundary for the far-field region is defined by the following inequality:

$$r > \frac{2D^2}{\lambda}, \tag{3.1}$$

where r denotes the distance from the antenna, D is the largest dimension of the antenna's aperture and λ is the wavelength of the radiated signal. It is important to note that D must be large compared to the wavelength (λ) for this expression to be valid [12].

3.2 Electric Far-Field Equations for a Rectangular Aperture in Free Space

The electric far-field radiated by an antenna behaves differently for different apertures and propagation environments. This study only considers rectangular apertures and assumes a uniform distribution of the electric field over the aperture in free space. Then, the electric far-field components can be described as:

$$E_\theta = \frac{C}{2}\sin(\phi)[1+\cos(\theta)]\frac{\sin(X)}{X}\frac{\sin(Y)}{Y}, \tag{3.2}$$

$$E_\phi = \frac{C}{2}\cos(\phi)[1+\cos(\theta)]\frac{\sin(X)}{X}\frac{\sin(Y)}{Y}, \tag{3.3}$$

with

$$X = \frac{ka}{2}\sin(\theta)\cos(\phi), \qquad Y = \frac{kb}{2}\sin(\theta)\sin(\phi) \qquad \text{and} \qquad C = j\frac{abkE_0e^{-jkr}}{2\pi r}. \tag{3.4}$$

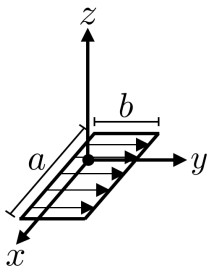

Figure 3.1: Rectangular aperture dimensions.

These expressions are taken from Table 12.2 in [12]. The variables a and b represent the aperture dimensions along the x- and y-axes respectively, as shown in Figure 3.1. Moreover, $k = \frac{2\pi}{\lambda}$ is the wave number, E_0 is the constant aperture field strength, r is the distance from the antenna and θ and ϕ are the elevation and azimuth angle, respectively.

These equations can be used to model the electric far-field components E_θ and E_ϕ. This is essential for analysing the characteristics of an antenna, such as the radiation pattern and directivity.

3.3 Radiation Pattern

The radiation pattern of an antenna describes how it radiates energy into space and is fundamental to understanding its performance and suitability for specific applications [13]. If the radiation pattern can be derived analytically, it is often expressed as a mathematical function. Otherwise, it can be determined numerically. In both cases, the pattern can be visualised graphically to aid interpretation.

One way to express the radiation pattern analytically is through the radiation intensity. This quantifies how much power the antenna sends out in a particular direction. It is defined as:

$$U(\theta, \phi) = \frac{r^2}{2\eta}(|E_\theta|^2 + |E_\phi|^2), \tag{3.5}$$

where $U(\theta, \phi)$ denotes the radiation intensity as a function of the elevation angle (θ) and azimuth angle (ϕ), E_θ and E_ϕ are the the far-field components of the electric-field and η is the intrinsic impedance of the propagation medium. The radial component of the electric-field is omitted, as it is assumed to be negligble in the far-field [12].

To interpret and compare antenna radiation patterns, it is useful to make a U-V plot. This offers a compact 2D visualisation of the 3D radiation pattern. This transformation is achieved by mapping the spherical coordinates to:

$$U = \sin\theta\cos\phi, \quad V = \sin\theta\sin\phi.$$

An example of a U-V plot of the radiation pattern is given in Figure 3.2. This pattern is generated using the electric far-field equations in (3.2) - (3.4), assuming a uniform current distribution over a rectangular aperture of size $a \times b$, with $a = b = 3\lambda$, $r = 1$m and at a frequency of 1 GHz. The equations model the radiation pattern produced by equivalent electric and magnetic currents (Huygens' sources), uniformly distributed across the aperture. The resulting plot shows the directional characteristics of the far-field radiation in U-V space.

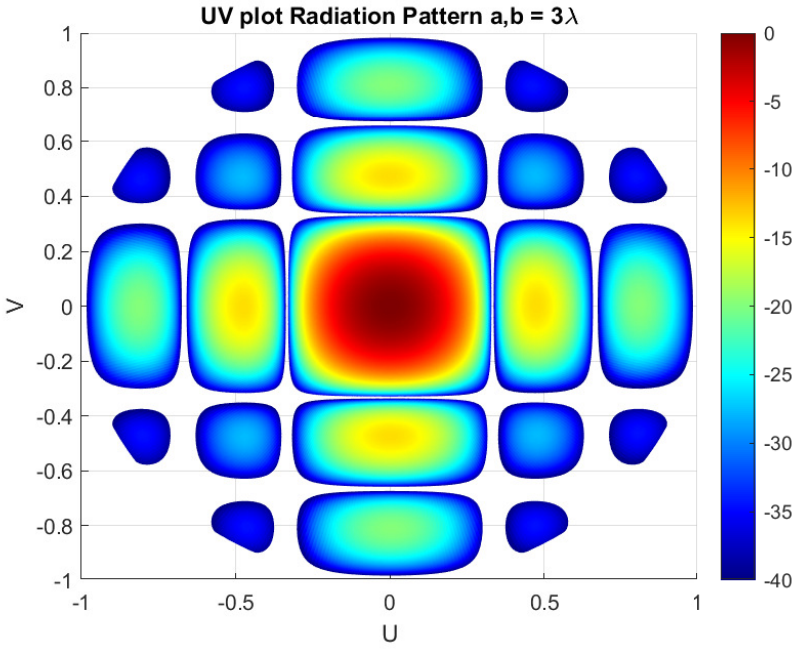

Figure 3.2: Normalised radiation intensity (in dB) of a uniform distribution apperture in free space.

The total radiated power P_{rad} can be obtained by integrating the radiation intensity over the surface of a sphere:

$$P_{\text{rad}} = \int_0^{2\pi} \int_0^{\pi} U(\theta, \phi) \sin(\theta) d\theta d\phi. \tag{3.6}$$

3.4 Directivity

Directivity is a key parameter that quantifies how focused an antenna's radiation pattern is in a particular direction. It compares the radiation intensity in the direction of maximum radiation to the total radiation intensity over all directions. In essence, directivity provides a measure of how effectively an antenna concentrates radiated power [12].

Using the radiation intensity defined in (3.5) and the total radiated power from (3.6), the directivity can be computed as:

$$D_0 = \frac{4\pi U_{\text{max}}}{P_{\text{rad}}} \tag{3.7}$$

where D_0 is the maximum directivity, U_{max} is the maximum value of the radiation intensity, and P_{rad} is the total radiated power. A higher directivity indicates that more power is radiated in a specific direction [12].

For antennas with sufficiently large apertures, the directivity can also be approximated analytically based solely on the physical aperture size. The simplified expression is given by:

$$D_0 = \frac{4\pi}{\lambda^2} A_p \tag{3.8}$$

where λ is the wavelength and A_p is the effective aperture area of the antenna [14].

This relation is illustrated by the graph in Figure 3.3, where the directivity is calculated for a range of aperture sized using both the exact formula in (3.7) and the analytical approximation in (3.8). The plot demonstrates that the analytical model aligns closely with the numerical integration, especially for larger apertures, validating the accuracy of the approximation in practical design scenarios.

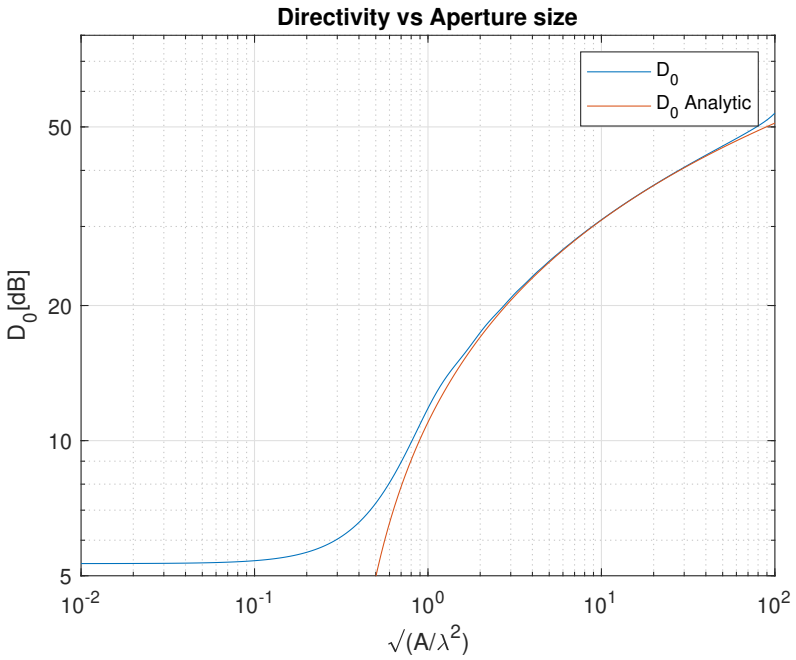

Figure 3.3: Directivity as a function of antenna aperture size.

3.5 Measuring the Electric Far-Field

While the electric far-field can be directly modeled using equations (3.2)–(3.4), and is used in the trade-off study presented in Chapter 5, it cannot be directly measured in practice using a VNA. This becomes especially relevant in the context of experimental validation, as discussed in Chapter 6.

Instead of measuring the electric far-field components E_θ and E_ϕ directly, the VNA measures voltages at its ports and computes the corresponding scattering parameters (S-parameters). Here, we are particularly interested in the S_{12} parameter, which represents the ratio of the reflected voltage wave at port 1 to the incident voltage wave at port 2, under the condition that $V_1^+ = 0$. This is given by:

$$S_{12} = \left.\frac{V_1^-}{V_2^+}\right|_{V_1^+=0}, \tag{3.9}$$

where V_n^+ is the amplitude of the voltage wave incident on port n, and V_n^- is the amplitude of the voltage wave reflected from port n (for $n = 1, 2$) [15].

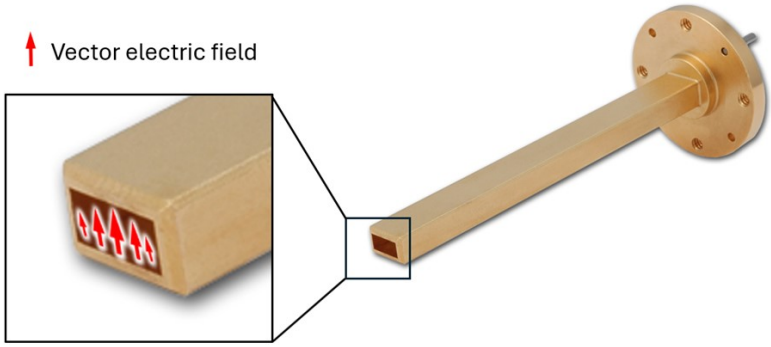

Figure 3.4: Example of the electric field in a rectangular aperture.

The received voltage at port 1 is proportional to the electric field component entering the waveguide probe at port 1 and aligned with the waveguides orientation. An illustration of the electric field distribution in a rectangular waveguide is shown in Figure 3.4.

Thus, the S_{12} measurement effectively captures the projection of the antenna's radiated field onto the polarisation of the receiving probe at its physical location. This makes S_{12} a practical and reliable quantity for experimental far-field characterisation.

These measurements are performed in terms of co-polarisation and cross-polarisation, which refer to the component of the radiated field aligned with the desired polarisation and the orthogonal (unwanted) component, respectively [16].

Chapter 4
Sampling Methods

This chapter provides a detailed discussion of various sampling methods considered in this thesis, including the traditional theta–phi grid, the Fibonacci grid, and the Gauss–Legendre quadrature.

4.1 Equiangular

The equiangular grid is a sampling grid for which the phi (ϕ) and theta (θ) angles are both uniformly distributed. For the full spherical grid, θ ranges from 0 to π and ϕ ranges from 0 to 2π. The number of points used for the equiangular grid depends on the stepsize δ between the grid lines, as $\delta = 180°/k$ with $k = 1, 2, ...$ denoting the number of grid lines. Then, $P = 2k(k-1)+2$, which comes down to the number of meridians ($2k$) times the number of parallels ($k-1$), plus the two poles [8]. The grid is thus independent of frequency and aperture size. An example of the grid can be seen in 4.1 and is widely used for sampling radiation patterns as it has a good accuracy, but lacks some efficiency and robustness [17]. The MATLAB function to generate this grid can be found in Appendix A.

For the equiangular grid, the total radiated power integral in (3.6) can be computed numerically, as $d\theta$ and $d\phi$ are known.

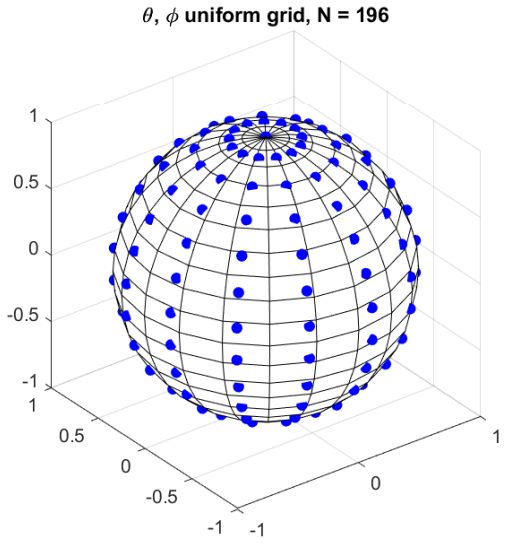

Figure 4.1: Theta Phi grid for N = 196.

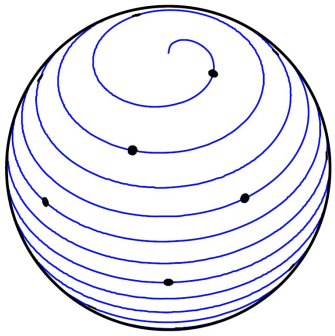

(a) Fibonacci spiral where the angular increment between successive points is derived from the golden angle [8].

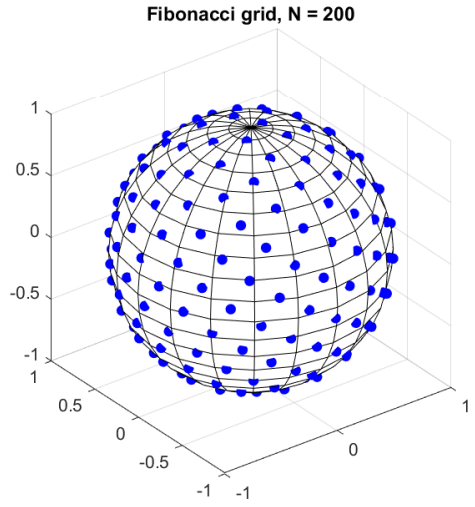

(b) Fibonacci grid for N = 200.

Figure 4.2: Comparison of Fibonacci spiral and Fibonacci grid.

4.2 Fibonacci

The Fibonacci grid distributes points along a spiral on the sphere's surface, where the angular increment between successive points is derived from the golden angle (see Figure 4.2a). The golden angle is given by

$$360^\circ \Phi^{-2} \simeq 137.5^\circ,$$

which is based on the golden ratio ($\Phi = 1 + \Phi^{-1} = (1 + \sqrt{5})/2 \simeq 1.618$). This results in a near-uniform distribution that reduces clustering and ensures more consistent spatial coverage [6], [7], [8].

The Fibonacci grid can be generated for $P = 2N + 1$ points, where $N \in \mathbb{N}$. The spherical coordinates of a point $i \in [-N, N]$ are given by

$$\begin{aligned} \theta_i &= \frac{\pi}{2} + \arcsin\left(\frac{2i}{2N+1}\right), \\ \phi_i &= 2\pi i \Phi^{-2}. \end{aligned} \tag{4.1}$$

An example of the grid is given in Figure 4.2b for $N = 200$. This means that $P = 2 \cdot 200 + 1 = 401$ points are placed on the sphere. Since these points are nearly uniformly distributed, the area (A) for each point can be approximated by the area of the sphere divided by the number of points on the sphere, i.e. $A = 4\pi/P$, where P the number of points.

The total radiated power (P_{rad}) would then easily be approximated by

$$P_{\text{rad}} \approx \frac{4\pi}{P} \sum_{i=1}^{P} U(\theta_i, \phi_i), \tag{4.2}$$

where $U(\cdot)$ denotes the radiation intensity. However, during simulations, it was observed that this method lacked sufficient accuracy, primarily because the point distribution is not perfectly uniform, especially near the poles.

To improve the approximation, it was noted that $d\theta$ could be numerically estimated by taking the difference between consecutive points and $d\phi$ could be approximated by $d\phi \approx 2\pi/P$, where P denotes the number of points on the sphere. The total radiated power can then be evaluated using (4.3).

The MATLAB function to generate this grid can be found in Appendix A.

$$\begin{aligned} P_{\text{rad}} &\approx \sum_{i=1}^{P} U(\theta_i, \phi_i) \sin\theta_i d\theta_i d\phi_i, \\ \text{with} \quad d\theta_i = \theta_i - \theta_{i-1} \quad &\text{and} \quad d\phi_i \approx \frac{2\pi}{P}. \end{aligned} \tag{4.3}$$

4.3 Gauss-Legendre

The Gauss-Legendre grid is generated using the Gaussian quadrature for approximating the integral performed on the Equidistant sphere integral. This means that the Gaussian quadrature is used for every phi and that the the integration in phi is a uniform one. The integral to calculate the radiated power is then approximated by a summation of polynomials multiplied with different weights [18]. The approximation is done using the following equation.

$$\int_{-1}^{1} f(x)dx = \sum_{i=1}^{n} w_i f(x_i) \tag{4.4}$$

This approximation can then be used to rewrite the integral for radiated power (P_{rad}), with a change of variables.

$$P_{\text{rad}} \approx w^{\phi} \sum_{j=1}^{Q_\phi} \sum_{i=1}^{Q_\theta} w_i^{\theta} U(\arccos(\gamma_i), \phi_j), \tag{4.5}$$

where the weights can be calculated using

$$\phi_j = \frac{2\pi(j-1)}{Q_\phi}, \tag{4.6}$$

$$w^{\phi} = \frac{2\pi}{Q_\theta}. \tag{4.7}$$

The gauss weights, w_i^{θ} and the gauss points γ_i are calculated using a MATLAB function present in Appendix A.

The number of points in θ and ϕ are calculated using the dimension of the antenna, D and the decimal precision d_0. Using the equations

$$Q_\theta = \frac{L+1}{2}, \tag{4.8}$$

$$Q_\phi = L + 1, \tag{4.9}$$

where L is calculated using

$$L = kD + 1.8 d_0^{2/3} (kD)^{1/3} \tag{4.10}$$

as stated in [18] and [19].

This summation will accurately approximate the equiangular grid with a significant reduction in sampling points [19],[20]. The resulting sampling grid is uniform in θ and ϕ. The number of points is only dependent on the decimal precision, d_0 and the size of the antenna, D. The decimal precision is set to one as this had negligible effect on the accuracy of the directivity calculations. A higher precision will increase the number of points and thus the measurement time of the grid. An example grid is shown in 4.3. The MATLAB to generate this grid can be found in Appendix B.

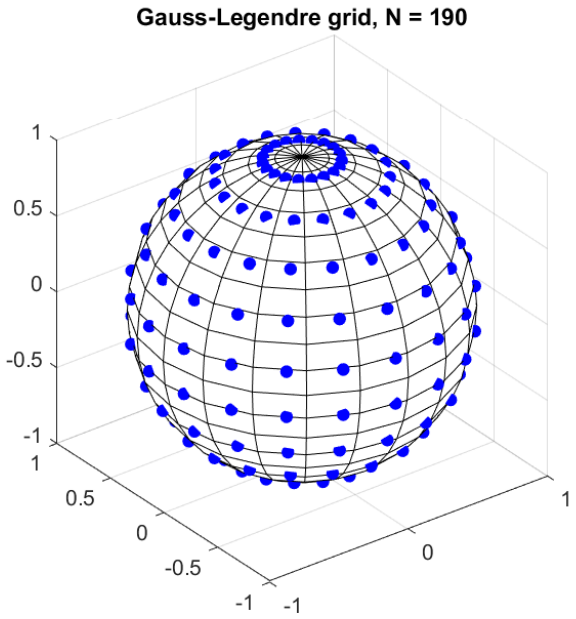

Figure 4.3: Gauss-Legendre for N = 190, $d_0 = 1$, a,b = 3 λ.

Chapter 5
Trade-off Study Based on Simulations

5.1 Description

The cost of a sampling scheme is defined by the time it takes to measure all points on the grid. The time is determined by the number of points in the grid. More points will require more measurements and more total time to move between the points. To determine the minimum number of points necessary, the sampling efficiency needs to be studied for different sampling schemes. This study was performed for the equiangular, Gauss-Legendre and Fibonacci grids. The antenna aperture used in this study was that of a uniform distribution aperture in free space as given in [12].

5.1.1 Sampling Efficiency

The sampling efficiency of a sampling grid is determined by the minimum number of sampling points necessary in order to accurately calculate the directivity. The accuracy is determined by the relative error. The relative error in this case is defined as the relative difference in the calculated directivity for a sampling grid with number of samples N compared to the same sampling grid for a high enough number N. The equation for this error is given as.

$$\text{Error} = \frac{|D_{N_{\min}} - D_{N_{\max}}|}{D_{N_{\max}}} \tag{5.1}$$

Thus to estimate which sampling scheme has the best sampling efficiency the minimum number of sampling points is calculated for which the sampling scheme does not exceed this error. A study was then conducted to determine which sampling scheme will have the highest sampling efficiency for different antenna apertures.

The resulting plot from the study is shown in figure 5.1, where the antenna width is plotted against the minimum number of sampling points. The relative error threshold to achieve this plot was set to 0.5%. Meaning that when the calculated directivity reached an error higher than 0.5% the lowest number of sampling points is reached. This is plotted for the equiangular, Gauss-Legendre and Fibonacci grids.

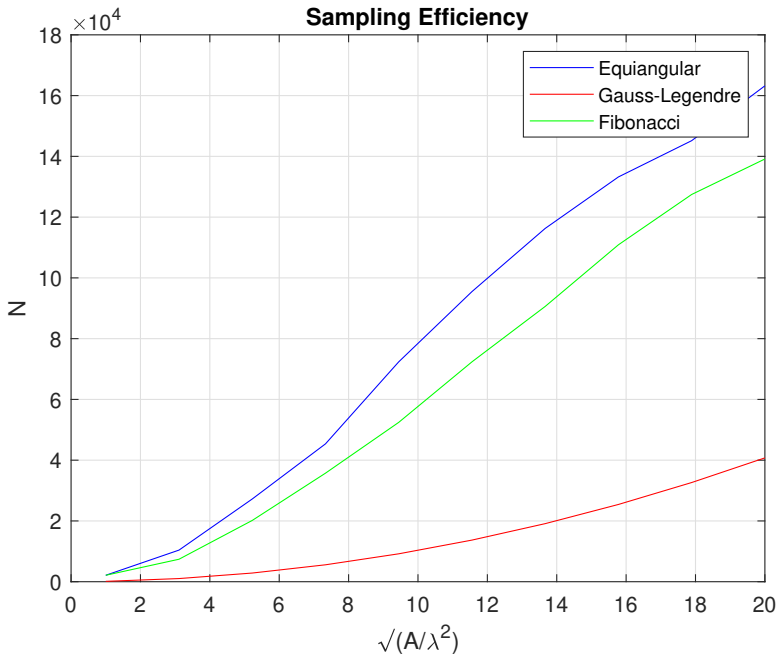

Figure 5.1: Number of samples for equiangular, Gauss-Legendre and Fibonacci sampling schemes.

From this plot the most efficient sampling grid can be concluded. For all antenna apertures the Gauss-Legendre sampling grid uses drastically less sampling points to achieve the same error in directivity. To compare for an aperture width of 5λ, an N of 2850, 13612 and 20165, is necessary for Gauss-Legendre, equiangular and Fibonacci respectively, for the full sphere grid. Something to note is that the number of points for the Fibonacci grid is quite high. The grid being just slightly more efficient than the standard equiangular grid. The grid is equidistant, meaning the distance between points is approximately equal. But by approximating the step size to be equal on all parts of the sphere the integral will have a high error, compared to other sampling grids. Some efforts were made to better approximate the step size, but this did not result in a higher sampling efficiency. Thus with this conclusion only the Gauss-Legendre and the equiangular grids were used in the measurement setup.

5.1.2 Sampling Scheme Truncation

A limitation of the measurement setup is that the robot arm is placed on a table, thus limiting it's maximum angle to $\theta = 90°$. In order to verify whether this angle is sufficient to accurately measure the radiation intensity using the grids mentioned in the previous paragraph, a study of this truncation angles effect on the accuracy was conducted.

The truncation angle is defined as the angle to which the grid's altitude angle is limited, as seen in Figure 5.2. In order to study the effect on the accuracy of the grid a definition for the accuracy must be agreed upon. The accuracy is here defined as the relative error of the sampling grid. The relative error for truncating the sampling grid is given by Equation (5.2).

$$\text{Error} = \frac{\left| \int_0^{2\pi} \int_0^{\theta_0} U \sin\theta d\theta d\phi - \int_0^{2\pi} \int_0^{\pi} U \sin\theta d\theta d\phi \right|}{\int_0^{2\pi} \int_0^{\pi} U \sin\theta d\theta d\phi} \tag{5.2}$$

Using this equation the relative error can be calculated for different truncation angles. This was done for the equiangular grid as this grid is uniform in θ and ϕ. For a range of aperture sizes to ensure the credibility of the study for different size antennas.

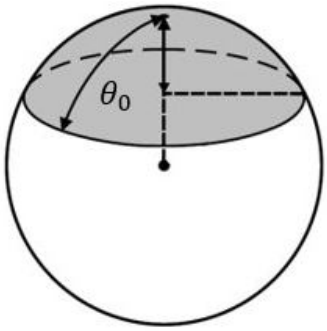

Figure 5.2: Truncation angle on a sphere.

The relative error contour plot is shown in Figure 5.3. The antenna size is plotted against the truncation angle, θ_0. The resulting contour plot shows the different contour lines for different error percentages. For example to achieve an error of 1% for an antenna width of 5λ a truncation angle of 50° is possible. The maximum truncation angle possible for this setup is 90° as this is the physical limitation of the robot arm on the table.

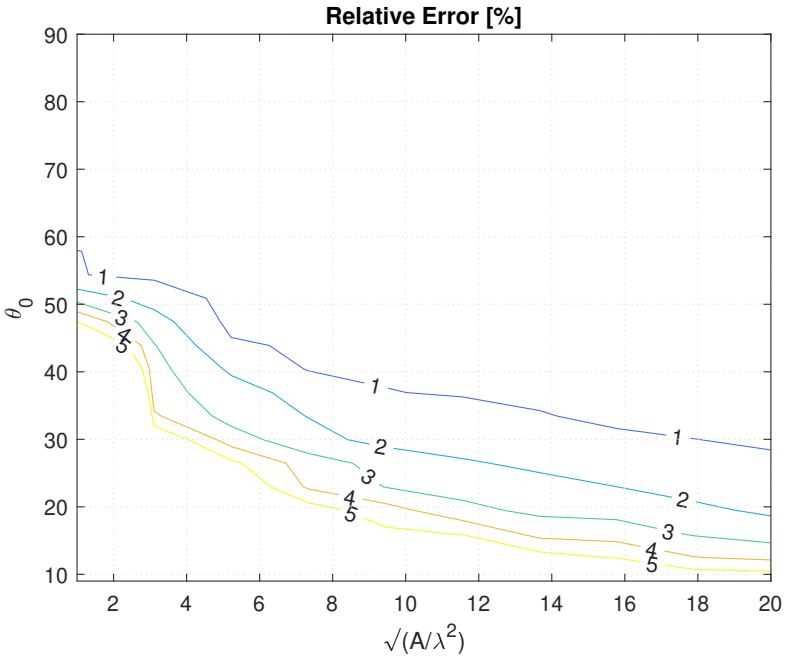

Figure 5.3: Relative error for truncated sampling schemes.

From the truncation plot an angle for the measurements can be concluded. The measurement setup uses a horn antenna with an aperture of between 2 and 3λ. For this aperture width a relative

error of between 2 and 3% an angle of 50° is chosen. The question can be raised as to why a larger angle isn't chosen to decrease the error even further and increase the accuracy. The way the grid is truncated makes it so that the number of sampling points will be lower for a smaller truncation angle. This in combination with the way the path the robot arm takes is chosen being more optimal for an angle of 50°, makes it so that this is the most efficient angle for the measurements. The final truncated grids used in these tests can be found in the Chapter 6.

Chapter 6
Experimental Validation

6.1 Description

Measurements were performed in order to validate the performance of the grids. The most optimal grids concluded from the trade-off study were tested on the measurement setup. These are the equiangular and the Gauss-Legendre grids. The number of points and truncation angle were chosen based on the results of the trade off study and the physical limitations of the measurement setup.

6.2 Measurement Setup

The grids were integrated into a Graphical User Interface (GUI) for an easy user interface. From this GUI the robot was sent the grid were it was sorted and the measurements were done using a path finding algorithm. The GUI and robot arm control operations were developed by the other subgroups in this BAP project. The limitations for this setup were the time it takes to measure a certain amount of points and the angle which the robot arm can reach. The effect of these limitations on the measurement grid are explained in the trade-off study in Chapter 5. The chosen antenna for the measurements is a horn antenna with an aperture size of $a = 2.65\lambda$, $b = 1.77\lambda$ and $a = 4\lambda$, $b = 2.67\lambda$ for 26.5 and 40 GHz, respectively. The horn was mounted on the optical table, its orientation being directly pointing up in the z-axis. The probe was an open ended waveguide to measure the two components of the field. The frequency sweep for which the measurements were made was 26.5 to 40 GHz. The final measurement setup is shown in Figure 6.1.

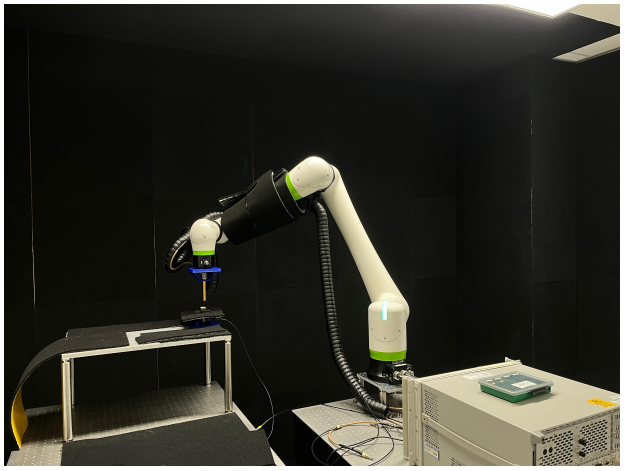

Figure 6.1: Measurement setup for spherical grids.

6.2.1 Equiangular Setup

For the equiangular grid used in the validation experiment, the number of points was chosen to be $N = 1161$. For a final truncation of 50° and an $r = 174mm$, as this was defined to be an wide enough radius for the measurement grid to be in the far-field region as specified in Section 3.1. A MATLAB function that calculates the distance to the far-field region is included in Appendix A.

This equiangular grid used in the measurement can be seen in Figure 6.2

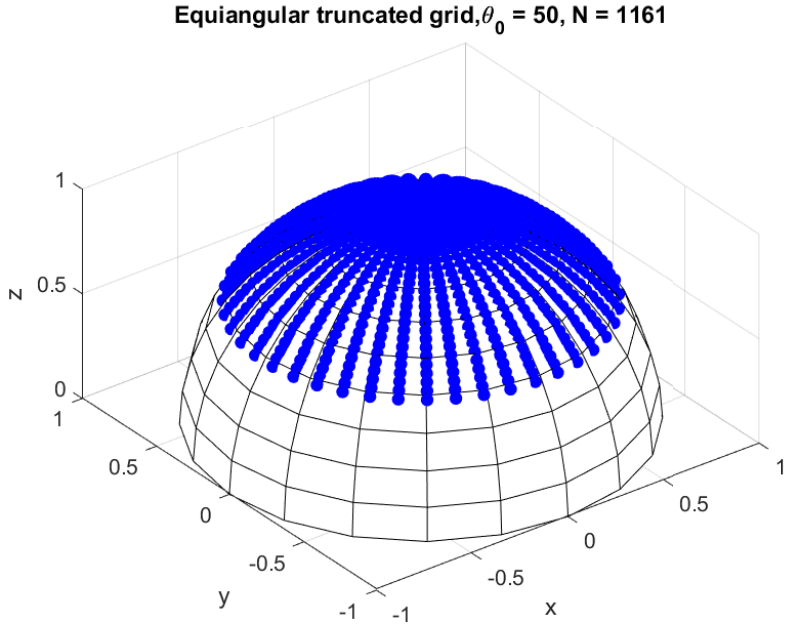

Figure 6.2: equiangular measurement grid.

6.2.2 Gauss-Legendre Setup

For the Gauss-Legendre grid used in the validation experiment, the number of points was chosen to be $N = 343$. For a final truncation of 50 ° and $r = 174mm$, see Figure 6.3. The truncation angle and radius were chosen in the same way as for the equiangular grid. The decimal precision, $d_0 = 1$ as explained in Chapter 4.

For the Gauss-Legendre grid three points were not measured, as the robot arm did not have a valid path to these points. The field at these three points were not measured and for the calculation set to zero. This had negligible effect on the calculation of the directivity, as the three missing points were well into the expected error range.

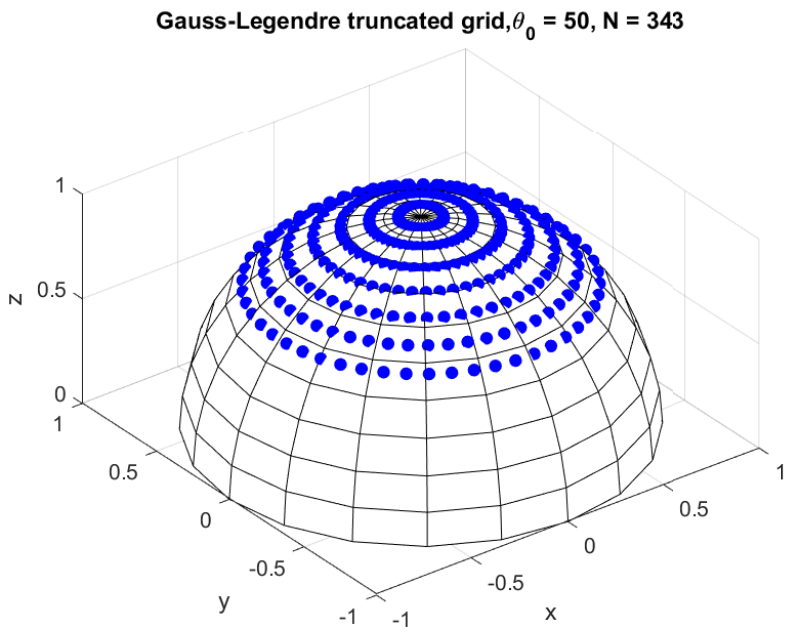

Figure 6.3: Gauss-Legendre for $N = 190$, $d_0 = 1$.

6.3 Results

For each point the cross- and co-polarisations were measured. The time it takes for a single measurement is 3-4 seconds per measuring point. This is the time it takes to measure both the cross and the co for all frequencies in the sweep. The time it takes to move between points is around 3-4 seconds, thus the total time per point is around 8 seconds. For the equiangular grid the estimated time then totals to 1161 * 8 = 9288 seconds, which is around 2.5 hours. For the Gauss-Legendre grid the time per point is equal as the cross and the co is measured in the same way and the algorithm the robot uses to move between points is identical. So the estimated time for the Gauss-Legendre grid totals to 343 * 8 = 2744, which is around 46 minutes.

6.3.1 Equiangular

Using the equiangular grid the radiation pattern was then measured, plotted and the directivity calculated. The measured fields can be seen in Figures 6.4 and 6.5, for the co- and cross-polarisation respectively.

Visible in the pattern is a cut around $\phi = 2\pi$ and the missing points omitted by the robot path algorithm. The missing points are explained in the previous paragraph and the cut is due to the measurement range for being from $\phi = 0$ to $\phi = 2\pi$. In this plot the side lobes and the main lobe are clearly visible in the radiation pattern.

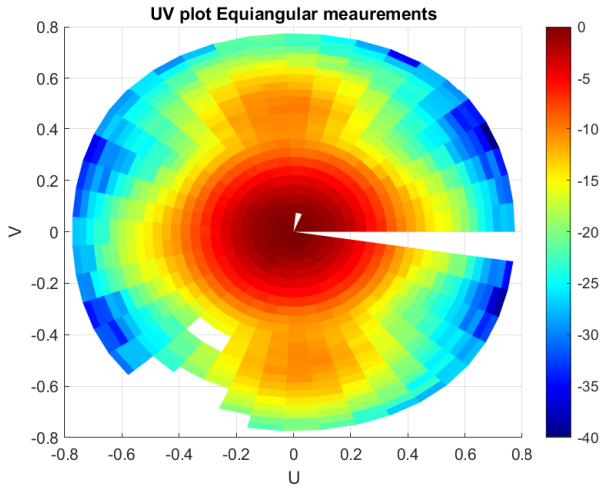

Figure 6.4: Normalised radiation intensity (in dB) of the co- polarisation field measured with the equiangular grid, f = 40 GHz.

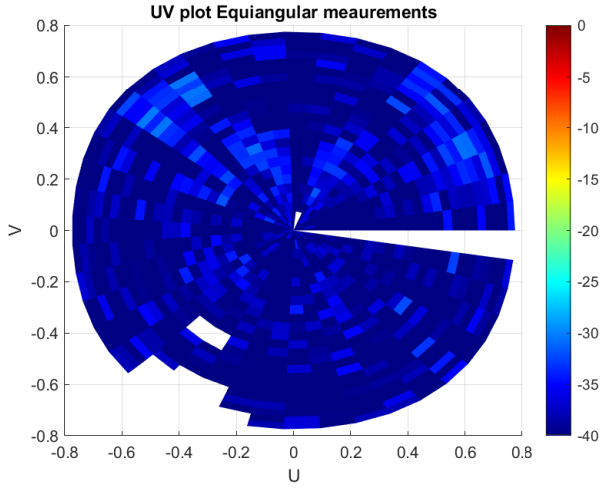

Figure 6.5: Normalised radiation intensity (in dB) of the cross-polarisation field measured with the equiangular grid, f = 40 GHz.

6.3.2 Gauss-Legendre

Using the Gauss-Legendre grid the radiation pattern was also measured in order to validate the grid with reduced number of samples. The resulting measured field can be seen in Figures 6.6 and 6.7, for the co- and cross-polarisation, respectively.

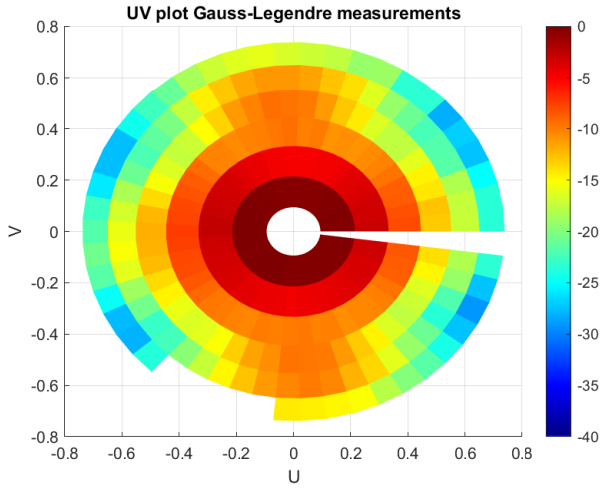

Figure 6.6: Normalised radiation intensity (in dB) of the co-polarisation field measured with the Gauss-Legendre grid, f = 40 GHz.

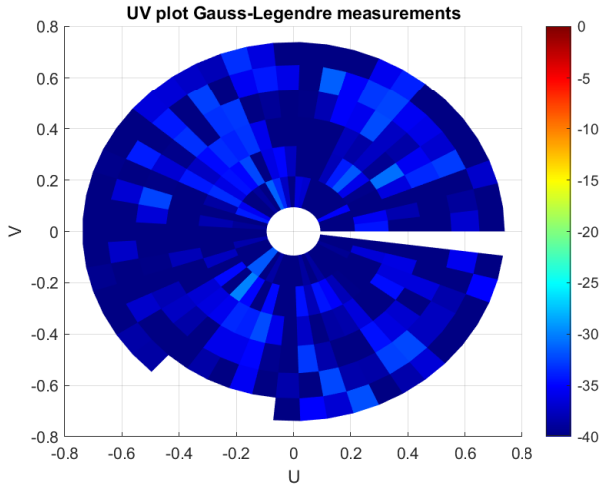

Figure 6.7: Normalised radiation intensity (in dB) of the cross-polarisation field measured with the Gauss-Legendre grid, f = 40 GHz.

Visible also in this pattern is the cut around $\phi = 2\pi$ and the missing points, these exist for the same reasons as for the equiangular grid. In this plot the side and main lobes are visible, but due to the reduced number of points the resolution of the plot is worsened and the patten is displayed less clearly.

6.3.3 Directivity Cuts

From these field measurements the directivity was calculated for different ϕ cuts for both the cross- and co-polarisation. These cuts, and also the cuts for the simulated data, for the different ϕ values can be seen in Figure 6.8.

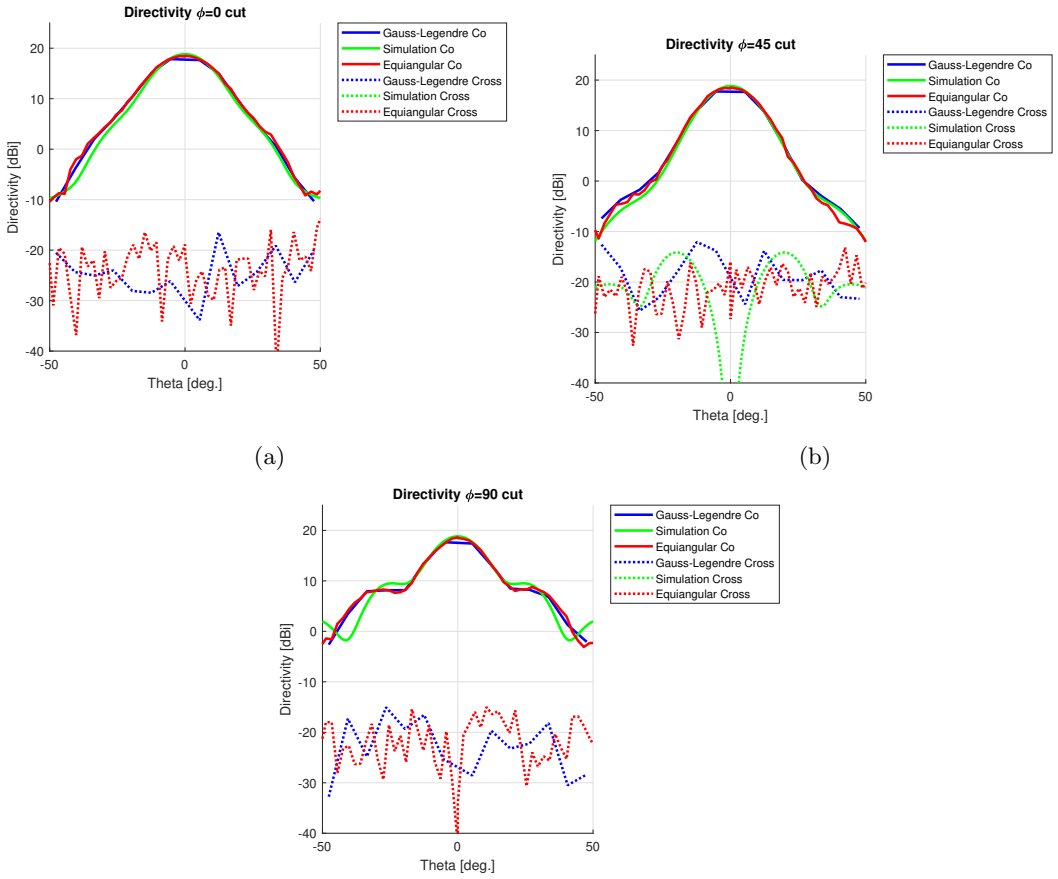

Figure 6.8: Directivity cuts for simulated, Gauss-Legendre and equiangular with $f = 40$ GHz, for (a) $\phi = 0°$, (b) $\phi = 45°$ and (c) $\phi = 90°$.

The co-polarisation directivity plots for all cuts are quite similar for each of the grids and the simulation. There is some small difference between the simulated directivity and the directivity calculated from the measurements. The cross-polarisation does not seem quite correct for any of the cuts. The $\phi = 45°$ plot shows some lobes for the cross-polarisation for the simulated plot, which the measured plots do not show. This is likely due to the noise being to high in the measurement to accurately measure the low power of the cross-polarisation. In the $\phi = 90°$ plot the side lobes are also visible next to the main lobe.

Chapter 7
Conclusion and Future Recommendations

In this thesis a study was performed to find the optimal algorithm for data acquisition in the far-field region. In order to find this optimal algorithm, some standard had to be set in order to say whether the algorithm is efficient and has reached a high enough accuracy. For the efficiency the cost was defined as the number of sampling points used in the sampling grid, as the limiting factor was the time it takes to measure the grid. For the accuracy the directivity was proposed as this is a property of the radiation pattern radiated by the antenna that can clearly be calculated and defined. And importantly compared between sampling grids. Finally the truncation of the grid, necessary due to physical limitations of the robot arm, was simulated and validated for experimental measurements.

For the sampling method, three different grids were investigated, equiangular, uniform in θ and ϕ, Gauss-Legendre, a more efficient form of integration applied to the equiangular grid and Fibonacci, which generates an equidistant grid. Simulations provided a clear understanding of the performance of each of the grids on a uniform distribution aperture. Here the Gauss-Legendre grid clearly outperformed both the equiangular and the Fibonacci grid. With the Fibonacci grid reaching only slightly higher efficiency than the equiangular grid. The simulation of the truncated grids resulted in clear overview of the effect of the angles on the accuracy of the grid. This resulted in a valid truncation angle of $\theta_0 = 50^\circ$ being found for a relative error of 0.5%, for both the equiangular and Gauss-Legendre grid.

In order to validate the results found in the simulations the grids were used in the measurement setup. In these measurements both the equiangular grid and Gauss-Legendre grid were used, where the equiangular grid provided a clear baseline for the performance. The radiation patterns from these measurements matched with those simulated and both the grids performed well in these measurements, with the more efficient Gauss-Legendre grid matching the equiangular one in accuracy. The directivity for the co-polarisation matched that of the simulated antenna aperture, the cross-polarisation however suffered from high background noise. This resulted in the low-power field of the cross-polarisation not being accurately measured.

In the beginning of this thesis a program of requirements was set out. In these requirements a set of requirements were specified specific to our Subgroup. These requirements are divided into functional requirements and system requirements. In the end all of the functional and system requirements were met. With the subsystem both performing as an individual system to calculate the directivity for simulated radiation patterns as well as integrated into the total measurement system. All methods set out were compared and the performance of these methods evaluated. The results were in line with the expectations at the beginning and resulted in a functional measurement setup that lives up to the standard set out at the beginning.

The part that lacked a satisfying result was the Fibonacci grid. The performance was not as

expected and the implementation could be improved. Specifically the approximation of the step size in the integral. The approximation used in this thesis resulted in a high error for the calculation of the directivity and thus a lower accuracy in combination with a higher number of sampling points needed. It would be interesting to see how it would perform if the integral was approximated using Voronoi cells, as mentioned in [21].

Another possible future improvement would be the simulation and validation for a setup where the antenna is not directly aligned with the probe. For an antenna which has a different angle compared to the probe the main lobes will be in a different position and thus the grid will need to be positioned differently compared to this new angle. A study on the robustness of the sampling schemes might yield some interesting results and other conclusion as to what the optimal algorithm is.

A future recommendation to improve the measurements of the cross-polarisation might be to time gate the measurements to remove some of the reflections present in the current measurements, a way to do this would be to perform differential measurement proposed by Dausien et al. [22].

Bibliography

[1] L. Boehm, F. Boegelsack, M. Hitzler, and C. Waldschmidt, "An automated millimeter-wave antenna measurement setup using a robotic arm," in *2015 IEEE International Symposium on Antennas and Propagation & USNC/URSI National Radio Science Meeting*, 2015, pp. 2109–2110.

[2] M. Meng, A. Wu, Z. Stokesberry, T. Zhao, S. Y. Lee, and N. Ghalichechian, "Robotic radiation pattern measurement system for 6–110 GHz based in both near field and far field," in *2023 IEEE International Opportunity Research Scholars Symposium (ORSS)*, 2023, pp. 11–15.

[3] J. Gordon, "Robotic antenna measurements," 2023. [Online]. Available: https://tsapps.nist.gov/publication/get_pdf.cfm?pub_id=936351

[4] D. M. Lewis, J. Bommer, G. E. Hindman, and S. F. Gregson, "Traditional to modern antenna test environments: The impact of robotics and computational electromagnetic simulation on modern antenna measurements," in *2021 15th European Conference on Antennas and Propagation (EuCAP)*, 2021, pp. 1–5.

[5] U. Ahmed and Z. Khalid, "Sampling schemes for accurate reconstruction and computation of performance parameters of antenna radiation pattern," in *ICASSP 2019 - 2019 IEEE International Conference on Acoustics, Speech and Signal Processing (ICASSP)*, 2019, pp. 4639–4643.

[6] R. Swinbank and R. J. Purser, "Fibonacci grids: a novel approach to global modelling," *Quarterly Journal of the Royal Meteorological Society*, vol. 132, pp. 1769–1793, 2006.

[7] J. H. Hannay and J. F. Nye, "Fibonacci numerical integration on a sphere," *Journal of Physics A: Mathematical and General*, vol. 37, no. 48, p. 11591–11601, 2004.

[8] A. González, "Measurement of areas on a sphere using fibonacci and latitude–longitude lattices," *Mathematical Geosciences*, vol. 42, no. 1, p. 49–64, 2009.

[9] J. D. McEwen and Y. Wiaux, "A novel sampling theorem on the sphere," *IEEE Transactions on Signal Processing*, vol. 59, no. 12, p. 5876–5887, 2011.

[10] A. G. Doroshkevich, P. D. Naselsky, O. V. Verkhodanov, D. I. Novikov, V. I. Turchaninov, I. D. Novikov, P. R. Christensen, and L.-Y. Chiang, "Gauss–Legendre sky pixelization (GLESP) for CMB maps," *International Journal of Modern Physics D*, vol. 14, no. 02, p. 275–290, 2005.

[11] Z. Khalid, R. A. Kennedy, and J. D. McEwen, "An optimal-dimensionality sampling scheme on the sphere with fast spherical harmonic transforms," *IEEE Transactions on Signal Processing*, vol. 62, no. 17, pp. 4597–4610, 2014.

[12] C. A. Balanis, *Antenna Theory: Analysis and Design*. USA: Wiley-Interscience, 2005.

[13] F. Ulaby and U. Ravaioli, *Fundamentals of Applied Electromagnetics Global Edition*. Harlow: Pearson, 2022.

[14] P.-S. Kildal and S. R. Best, "Further investigations of fundamental directivity limitations of small antennas with and without ground planes," in *2008 IEEE Antennas and Propagation Society International Symposium*, 2008, pp. 1–4.

[15] D. M. Pozar, *Microwave Engineering*, 4th ed. Chichester, England: John Wiley & Sons, Nov. 2011.

[16] A. Ludwig, "The definition of cross polarization," *IEEE Transactions on Antennas and Propagation*, vol. 21, no. 1, pp. 116–119, 1973.

[17] J. A. Flint, S. Ullah, R. D. Seager, and S. C. Pomeroy, "Low resolution radiation pattern sampling for a thin dipole," in *2010 Loughborough Antennas & Propagation Conference*, 2010, pp. 601–604.

[18] R. Ozzola, R. G. Tapia Barroso, D. Cavallo, and A. Neto, "Study on the generation of independent beams from planar domains," in *17th European Conference on Antennas and Propagation*, Florence, Italy, Mar. 26 - 31 2023.

[19] A. Mazzinghi and A. Freni, "Analytical evaluation of the power radiated by sources arbitrarily distributed on a surface," *IEEE Transactions on Antennas and Propagation*, vol. 70, no. 12, pp. 12 376–12 380, 2022.

[20] C. H. L. Beentjes, "Quadrature on a spherical surface," 2016. [Online]. Available: https://api.semanticscholar.org/CorpusID:19681887

[21] B. Keinert, M. Innmann, M. Sänger, and M. Stamminger, "Spherical fibonacci mapping," *ACM Transactions on Graphics*, vol. 34, no. 6, p. 1–7, 2015.

[22] K. Dausien, T. Körner, C. Schulz, N. Pohl, I. Rolfes, and J. Barowski, "Ultrawideband millimeterwave robotic antenna measurements enabled by FMCW radar sensors," in *2025 19th European Conference on Antennas and Propagation (EuCAP)*, 2025, pp. 1–4.

Appendix A
Matlab Code

A.1 MATLAB Code for Generating Equiangular Grid

```
function Grid_Matrix = Theta_Phi_Grid(N, R, theta0)
% Generate a pose for planar or tilted planar scanning.
% INPUTS:
% - N    : N^2 number of sampling points
% - R    : Radius of sampling hemisphere, ideally where far field
    begins
%
% OUTPUT:
% - SamplingMatrix     : N^2x3 Homogeneous transformation matrix
%   -columns:theta,phi,R

%% Evaluate each point on the upper hemisphere

theta = linspace(eps, pi, N); % radian
M=round(N/2);
phi   = linspace(eps, 2* pi*(1-1/(M-1)), M);
[TH, PH] = meshgrid(theta, phi);
[~,ind]= min(abs(TH(1,:) - deg2rad(theta0)));


theta = reshape(TH(:,1:ind), [], 1);
phi = reshape(PH(:,1:ind), [], 1);

Grid_Matrix = zeros(length(phi),3);

Grid_Matrix(:,1) = theta;
Grid_Matrix(:,2) = phi;
Grid_Matrix(:,3) = R;

end
```

A.2 MATLAB Code for Generating Fibonacci Grid

```
function [phi,theta,dtheta,dphi,Npoints] = fibonacci_sphere(N,
    theta0)
% close all
%theta0 can be from 0 to pi
gr = 1.618;
i=[-N:-N + round(2*N*theta0/pi)];
P = 2*N+1;
theta = pi/2 + asin(2*i/P);
phi = 2*pi*i./gr.^2;

Npoints = length(i);

% % plot
%  r=1;
%  X = r*sin(theta).*cos(phi);
%  Y = r*sin(theta).*sin(phi);
%  Z = r*cos(theta);
%  sphere
%  caxis([-200,-100])
%  axis equal
%  colormap("gray")
%  hold on
%  scatter3(X,Y,Z,'bo','filled')
%  title(['Number of points: ' num2str(Npoints) ])


 %[phi_sort,ind] = sort(atan2(Y,X));
 dphi = 2*pi;
 % [PH,TH] = meshgrid(phi,theta);

 dtheta=theta(2:end)-theta(1:end-1);
 % sum(sum(sin(TH(2:end,:)).*dtheta.*dphi));
%  2*pi*(1-min(Z))
 end
```

A.3 MATLAB Code for Generating Gauss-Legendre Grid

```
function Grid_Matrix = GL_Grid(a,b,d0,f,theta0,R)
%UNTITLED3 Function to compute Gauss-Legendre sampling scheme
%   Detailed explanation goes here
c = physconst('LightSpeed'); % speed of light

%frequency dependent parameters
lam = c / f;
k = 2*pi / lam;
a = a * 1e-3
b = b * 1e-3
%compute diameter of antenna aperture
D = sqrt(a^2 + b^2);

%compute N of sampling points for theta and phi based on d0
L = round(k * D + 1.8 * d0 ^(2/3) * (k*D)^ 1/3);
Nthe = round((L + 1) / 2);
Nphi = L + 1;

wphi = 2* pi / Nphi;

phi_j  = linspace(1,Nphi,Nphi);
phi_j = 2*pi* (phi_j-1) /Nphi;

%compute Gauss points and weights
[x,w]=lgwt(Nthe,-1, 1);
theta_i = acos(x);
% [TH, PH] = meshgrid(theta_i, phi_j);
[PH, TH] = meshgrid(phi_j,theta_i);
[~,ind]= min(abs(TH(:,1) - deg2rad(theta0)));

theta = reshape(TH(1:ind,:), [], 1);
phi = reshape(PH(1:ind,:), [], 1);

Grid_Matrix = zeros(length(phi),4);

Grid_Matrix(:,1) = theta;
Grid_Matrix(:,2) = phi;
Grid_Matrix(:,3) = R;
Grid_Matrix(:,4) = wphi;

end
```

A.3.1 MATLAB Function for Generating Gauss Weights

```
function [x,w]=lgwt(N,a,b)

% lgwt.m
%
% This script is for computing definite integrals using Legendre-
    Gauss
% Quadrature. Computes the Legendre-Gauss nodes and weights  on an
     interval
% [a,b] with truncation order N
%
% Suppose you have a continuous function f(x) which is defined on
    [a,b]
% which you can evaluate at any x in [a,b]. Simply evaluate it at
    all of
% the values contained in the x vector to obtain a vector f. Then
    compute
% the definite integral using sum(f.*w);
%
% Written by Greg von Winckel - 02/25/2004
N=N-1;
N1=N+1; N2=N+2;

xu=linspace(-1,1,N1)';

% Initial guess
y=cos((2*(0:N)'+1)*pi/(2*N+2))+(0.27/N1)*sin(pi*xu*N/N2);

% Legendre-Gauss Vandermonde Matrix
L=zeros(N1,N2);

% Derivative of LGVM
Lp=zeros(N1,N2);

% Compute the zeros of the N+1 Legendre Polynomial
% using the recursion relation and the Newton-Raphson method

y0=2;

% Iterate until new points are uniformly within epsilon of old
    points
while max(abs(y-y0))>eps


    L(:,1)=1;
    Lp(:,1)=0;

    L(:,2)=y;
    Lp(:,2)=1;
```

```
    for k=2:N1
        L(:,k+1)=( (2*k-1)*y.*L(:,k)-(k-1)*L(:,k-1) )/k;
    end

    Lp=(N2)*( L(:,N1)-y.*L(:,N2) )./(1-y.^2);

    y0=y;
    y=y0-L(:,N2)./Lp;

end

% Linear map from[-1,1] to [a,b]
x=(a*(1-y)+b*(1+y))/2;

% Compute the weights
w=(b-a)./((1-y.^2).*Lp.^2)*(N2/N1)^2;
```

A.4 MATLAB Code for Calculating Far-Field Radius

```
function R = Far_Field_Distance(a, b, freq)
% Obtain the minimum radius for the Far-field region (Fraunhofer)
    in mm
freq_max = max(freq);
D_max = sqrt(a^2 + b^2)* 1e-3; % mm to m
lambda = physconst('LightSpeed')/freq_max;
R = 2 * D_max * D_max / lambda;
R = int64(ceil(R * 1e3));
end
```

A.5 MATLAB Code to Generate Far-Field for Uniform Distribution Aperture

```
function [U] = Far_Field(a,b,k,E0,R,eta,TH,PH)
%Implement Far field equations
%   Detailed explanation goes here
C = 1i*a*b*k*E0* exp(-1i*k*R) / (2*pi*R);

X = k*a/2 .* sin(TH) .* cos(PH);
Y = k*b/2 .* sin(TH) .* sin(PH);

Ethe = C/2 .* sin(PH) .* (1 + cos(TH)) .* sinc(X / pi) .* sinc(Y /
    pi);
Ephi = C/2 .* cos(PH) .* (1 + cos(TH)) .* sinc(X / pi) .* sinc(Y /
    pi);

U = 1/(2 * eta) * ((abs(Ethe).^2) + (abs(Ephi).^2));

end
```

Appendix B
Figures

B.1 Simulation Figures

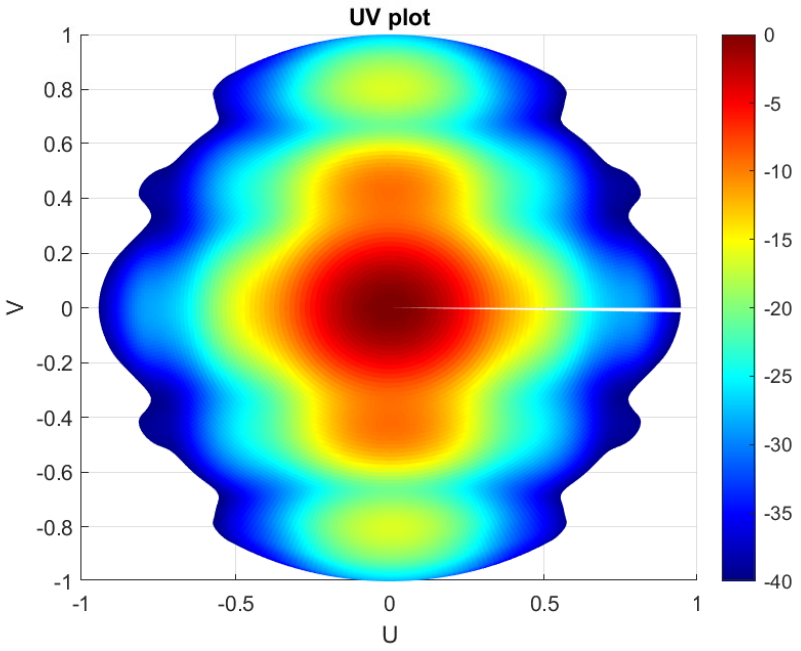

Figure B.1: Simulated Normalised radiation intensity (in dB) of a horn antenna distribution aperture in free space.

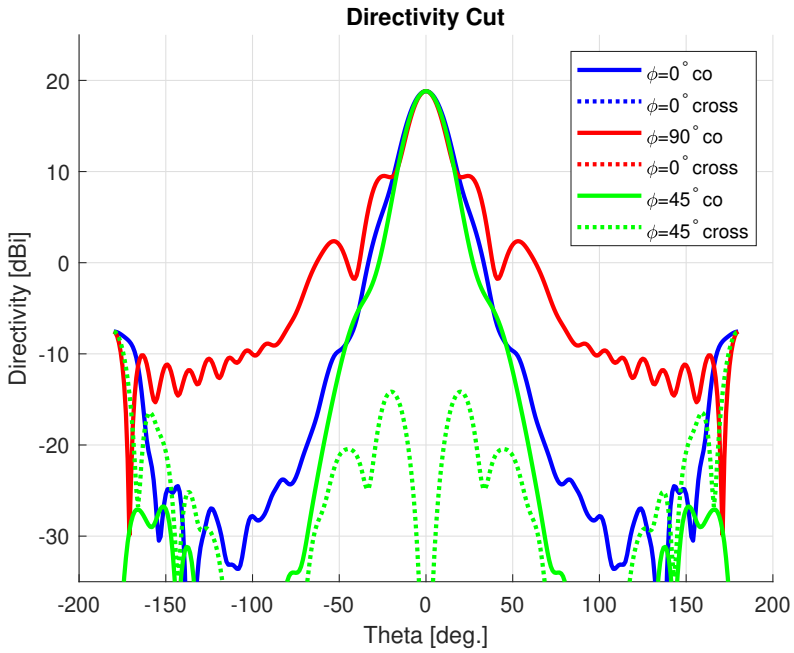

Figure B.2: Directivity cuts of the simulated data.

B.2 UV Plots With Sampling Grid Overlay

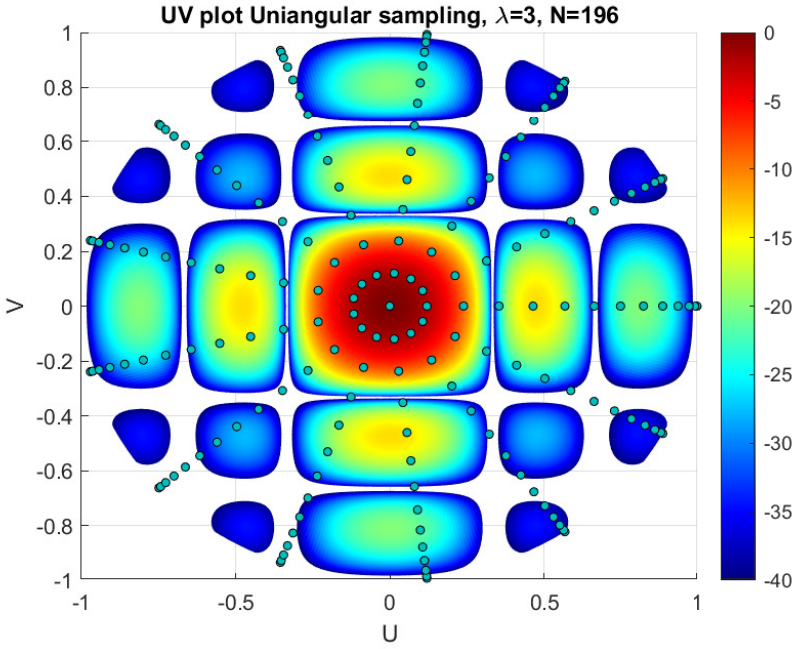

Figure B.3: UV plot with Equiangular sampling grid overlay.

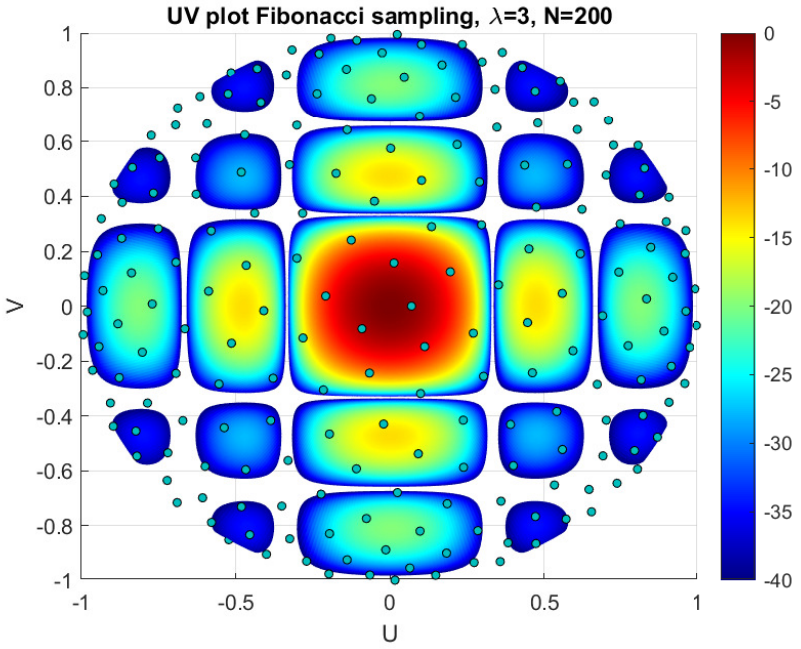

Figure B.4: UV plot with Fibonacci sampling grid overlay.

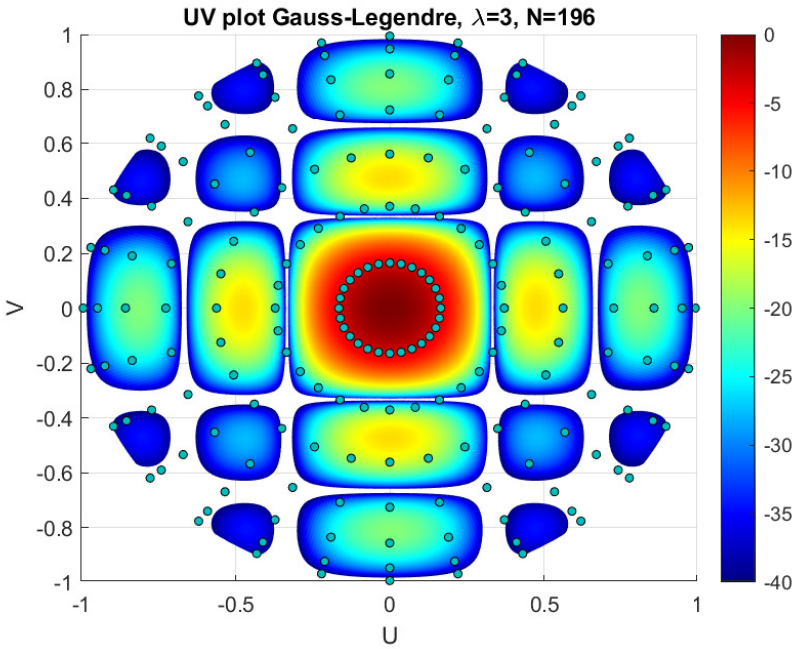

Figure B.5: UV plot with Gauss-Legendre sampling grid overlay.